# Two Keggin-Based Isostructural POMOF Hybrids: Synthesis, Crystal Structure, and Catalytic Properties

Soumyabrata Roy,[†,‡] Vamseedhara Vemuri,[†] Sthitadhi Maiti,[†] Kaja Sai Manoj,[†,‡] Udumula Subbarao,[†] and Sebastian C. Peter*,[†,‡] [ID]

[†]New Chemistry Unit and [‡]School of Advanced Materials, Jawaharlal Nehru Centre for Advanced Scientific Research, Bangalore 560 064, India

[S] *Supporting Information*

ABSTRACT: In this work we synthesized two novel isostructural twin hybrids **Comp1**: $[H(C_{10}H_{10}N_2)Cu_2][PMo_{12}O_{40}]$ & **Comp2**: $[H-(C_{10}H_{10}N_2)Cu_2][PW_{12}O_{40}]$, based on the Keggin ions ($PMo_{12}O_{40}^{-3}$ & $PW_{12}O_{40}^{-3}$), Cu(I) cation, and 4,4′-bipyridine, by in situ hydrothermal reduction of Cu, facilitated through extensive standardizations of synthetic pH conditions. Both compounds crystallized in monoclinic $P2_1/c$ space group with similar lattice parameters and crystal structures. The structural similarity prompted us to explore comparative catalytic properties of the hybrids, to understand the relative role of the POM species in the activity. While characterization techniques like powder X-ray diffraction (XRD), single-crystal XRD, IR, adsorption studies, etc. confirmed the identical structural hierarchy in the twin polyoxometalate-based metal organic frameworks (POMOFs), critical analyses through X-ray photoelectron spectroscopy, X-ray absorption near-edge structure spectroscopy, and magnetic property studies elucidated the electronic and local structural properties of the two. The hybrids were highly active for heterogeneous catalysis of small-molecule oxidation, with Comp 2 showing better activity than Comp1, particularly for oxidation of ethylbenzene and cyclooctene. Comp2 also outperformed Comp1 in photocatalytic degradation of methylene blue, with higher conversion efficiency of 83% and one order higher apparent rate constant of 0.0139 min^{-1}, which is comparable to that of the well-known photocatalyst, P25. Electrochemical pseudocapacitance studies revealed that these POMOFs are having the potential to act as good charge storage and conducting devices if their electrochemical stability can be improved.
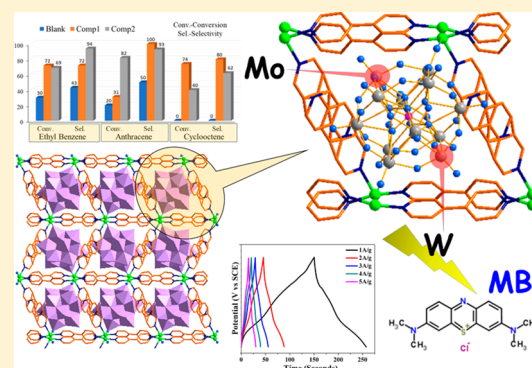
1. INTRODUCTION

Polyoxometalate-based metal−organic frameworks (PO-MOFs) are a class of emerging supramolecular hybrids that combine the functionalization properties of metal−organic frameworks (MOFs) with the rich physicochemical properties of polyoxometalates (POMs). On one hand, MOF research has seen an unprecedented growth in the last two decades and encompassed many other secondary research fields primarily due to their functionalized porous properties and applications in gas storage, magnetism, photochemistry, proton conduction, and catalysis.[1,2] POMs, on the other hand, are nanoclusters of early transition-metal (TM) oxides, having high anionic charge and oxygen-rich surface with a wide variety of sizes, compositions, and structures.[3,4] Chemistry of TMs, anionic nature, and surface oxygen renders POMs as highly active materials for catalysis, electrochemical applications, and rich photochemistry.[5−13] The rich redox chemistry of TMs incorporated into the rigid but chemically flexible nanoframe-work of POMs have found wide applications in the field of energy storage, photo- and electrocatalysis, organic catalysis, solar cells, supercapacitors, nonlinear optics, etc.[14−17] The hierarchical structures of the POMOFs fine-tune the structural

and electronic properties of the multifunctional hybrids and play a crucial role in determining their applications and efficiencies.[18] Synthesis and design of hierarchical assemblies like zero-dimensional (0D) open frameworks, one-dimensional (1D) chains, and two-dimensional (2D) nets, based on primary and secondary building units of basic MOF architectures and POMs, have started a new era of novel material design for targeted use in various fields ranging from material science to biomedicine. POMs due to their anionic nature and ligating oxygens are well-known inorganic ligands and act as building units of such hierarchical structures based on organic ligands and cationic secondary metal ions through covalent or noncovalent linkages.[19−23] The design of the organic ligands, the structural nature of the POM, and the coordination geometry of the secondary metal ions are the primary structure directing agents in the design of these hybrids. The use of organic ligands and secondary metal ions often enhances the rich redox chemistry of POMs through synergistic interactions to improve mechanical and chemical

stability, solubility, surface area, catalytic site segregation, electronic contributions, and photophysical and electrochemical effects.[24−27] Most of the POMOFs reported have exploited primarily two classes of classical heteropolyacids (HPAs) or their close derivatives, specifically, the Keggin $(XM_{12}O_{40}{}^{n-})$[25] and the Wells−Dawson units $(X_2M_{18}O_{62}{}^{n-})$.[27,28] However, recently there have also been several reports of other POMs (classical/nonclassical) used in extended or molecular frameworks (0D/1D/2D), e.g., basket-like POMs,[28] $P_6Mo_{18}O_{73}$,[29] Anderson $(XM_6O_{24}{}^{n-})$[30] decavanadate $(V_{10}O_{28}{}^{6-})$.[31]

POMs or POMOFs have been used as highly efficient catalysts for different catalytic reactions like acid-catalyzed reactions, selective oxidations, hydrogenation reactions, and also for industrial catalysis because of their oxygen-rich surface, nanodimensions, Bronsted acidity, and redox facile nature.[17,32−38] Of these different catalytic processes, partial oxidation of small organic molecules to selective products is of huge significance, as the end products are important for both pharmaceuticals and chemical industries for downstream processes. The primary challenge in the selective oxidation of these molecules is to arrest the desired end products at a partially oxidized state, where there are more thermodynamically favored products at the upstream of further oxidations. Thus, the need for conversion of precursors to the desired products, arresting the reactions at non-thermodynamic or sometimes nonkinetic states, necessitates the use of suitable catalysts, which can guide the reaction through optimum pathways. HPAs, because of their rich properties mentioned earlier, have efficiently catered to this particular catalytic need since its very advent, several decades ago. The major obstacle before using the HPAs in extensive catalytic applications is their high solubility in all polar solvents (organic and aqueous), a property that originates from the same nature that renders POMs their catalytic richness.[39,40] Heterogenous catalysis has distinct advantages over homogeneous catalysis in terms of stability, separability, and recyclability.[41] Thus, to decouple solubility issues from benevolent properties, immobilization of POMs in the forms of POMOFs is perhaps the most suitable way among other methods, which include the use of ionic liquids, mesoporous materials, and water-insoluble salts of POMs (e.g., Cs+).[32,40,42,43]

Organic dyes are a class of environmental pollutants with severe health hazards that are ubiquitously used across several industries like that of rubber, textile, pharmaceutical, plastic, leather, paper and printing, etc.[44] These dyes even in dilute concentrations pose immense threat to water and environmental pollution due to their toxicity, potential mutagenicity, and carcinogenicity.[44−47] Thus, aqueous and other effluent wastes from such industries need serious treatment before being discharged. While there are several techniques for removing dye pollutants from wastewater like coagulation, oxidation, filtration, and flocculation,[44] photocatalytic degradation of dyes is one of the best renewable ways to solve the problem. POMOFs, combining the optical properties of ligands and redox/photoredox properties of POMs, are particularly attractive for such photocatalytic applications and thus have been extensively studied.[48] However, the search for better, more efficient, and stable photocatalysts still necessitates explorations of newer systems for photocatalytic dye degradation. Redox-rich POM-based hybrids have also been extensively used for various electrochemical studies[11] starting from energy storage,[12] water splitting,[49,50] and nitrite

reduction[51] to supercapacitance studies.[15] In this report, using in situ direct hydrothermal techniques, we synthesized two analogous and isostructural POMOFs, namely, **Comp1**: $[H(C_{10}H_{10}N_2)Cu_2][PMo_{12}O_{40}]$ & **Comp2**: $[H(C_{10}H_{10}N_2)Cu_2][PW_{12}O_{40}]$ based on the twin Keggin anions $(PMo_{12}O_{40}{}^{3-}$ & $PW_{12}O_{40}{}^{3-})$, 4,4′-bipyridine (4,4′-bp), and Cu^{1+} as the secondary metal cation. Structural characterization through single-crystal X-ray diffraction (SCXRD) studies revealed a similar structural disorder in both the hybrids, originating from the 4,4′-bp arrangement along the axis of the 1D Cu-bp (bp = bipyridine) chain. The compounds were extensively characterized through SCXRD, powder X-ray diffraction (PXRD), infrared spectroscopy (IR), and elemental analyses. Magnetic, X-ray photoelectron spectroscopy (XPS), and X-ray absorption near-edge spectroscopy (XANES) studies revealed the electronic and oxidation states of the metal ions in the compounds, which was proved to be +6 for Mo/W and +1 for Cu. The POMOFs were then tested for their heterogeneous, photocatalytic, and electrochemical properties. The compounds showed good catalytic activity for peroxide-mediated partial oxidation of small organic molecules like ethylbenzene, anthracene, cyclooctene, etc. UV−Vis spectroscopic studies showed that the compounds are semiconducting in nature with a band gap of 2.7−2.9 eV. The compounds also showed fast and efficient photodegradation of methylene blue dye under UV irradiation. Exploration of electrochemical properties of the compounds showed that the compounds are active for electrochemical nitrite reduction and have pseudocapacitive properties. Thus, these two POMOFs exhibited the classic case of synergistic enhancement of various catalytic properties in hybrids, originating from two subunits, which had their own shortcomings.

2. EXPERIMENTAL SECTION

2.1. Materials. The chemicals were obtained from already available commercially certified reagent sources and were used without any further purifications unless mentioned. Sodium molybdate dihydrate ($Na_2MoO_4·2H_2O$, analytical reagent (AR), 99%), cupric chloride dihydrate ($CuCl_2·2H_2O$, AR, 99.9%), and concentrated (conc) HCl were purchased from SDFCL. 4,4′-Bipyridyl (($C_{10}H_8N_2$), AR) and glacial acetic acid (CH_3COOH, 16 N, 99.99%) were purchased from Sigma-Aldrich. Disodium hydrogen phosphate dihydrate ($Na_2HPO_4·2H_2O$, AR) was bought from Merck.

2.2. Synthesis. *Comp1-[H(C₁₀H₁₀N₂)Cu₂][PMo₁₂O₄₀].* The polyoxometalate-based inorganic−organic hybrid materials were synthesized using hydrothermal method. The 50 mL Teflon autoclaves were filled with 35 mL of distilled water (70% volume capacity) followed by the addition of 0.5 g (2.07 mmol) of $Na_2MoO_4·2H_2O$ while stirring. The pH of the solution was maintained between 4 and 5 by adding 10−15 drops of 16 N glacial acetic acid dropwise. Na_2HPO_4 (0.42 g, 1.391 mmol) was added to the reaction mixture, and again 15 drops of 17.4 N glacial acetic acid was added to the solution to maintain the pH between 4 and 5. In the next step 0.238 g (1.396 mmol) of $CuCl_2·2H_2O$ and 0.268 g (1.387 mmol) of 4,4′-bp were added, and the color of the solution turned greenish-blue. In the end 11 drops of conc HCl was added to adjust the pH close to 2. Finally, the reaction mixture was kept at 180 °C for a period of 5 days.

Comp2-[H(C₁₀H₁₀N₂)Cu₂][PW₁₂O₄₀]. The 50 mL Teflon autoclaves were filled with 35 mL of distilled water (70% volume capacity) followed by addition of 0.682 g (2.07 mmol) of $Na_2MoO_4·2H_2O$ while stirring. The pH of the solution was maintained between 4 and 5 by adding 10−15 drops of 16 N glacial acetic acid dropwise. Na_2HPO_4 (0.42 g, 2.356 mmol) was added to the reaction mixture, and again 15 drops of 16 N glacial acetic acid was added to the solution to maintain the pH between 4 and 5. In the next step 0.238 g (1.396 mmol) of $CuCl_2·2H_2O$ and 0.268 g (1.387 mmol) of 4,4′-bp

were added, and the color of the solution turned greenish-blue. In the end 11 drops of conc HCl was added to adjust the pH close to 2. Finally, the reaction mixture was kept at 180 °C, and the duration was 5 d.

The autoclaves were kept at 180 °C for 5 d, after which they were allowed to cool to room temperature over a period of 12 h. On cooling, dark red identical crystals were obtained for both the reactions, which were cleaned with distilled water and dried with acetone. The details of the reaction conditions are tabulated in Table S1.

2.3. Single-Crystal XRD. The crystals obtained from the hydrothermal reaction were used to collect the structural information using SCXRD technique. The XRD data were collected using Bruker Smart X2 APEX II CCD diffractometer with normal focus, 2.4 kW sealed tube X-ray source with graphite monochromatic Mo Kα radiation ($\lambda = 0.710\,73$ Å) operating at 50 kV and 30 mA, with ω scan mode. Suitable single crystals of the samples of both W and Mo were mounted on a thin glass fiber with commercially available super glue. The program SAINT[52] was used for integration of diffraction profiles, and absorption corrections were made with SADABS program.[53] All the structures were solved by direct method and followed by successive Fourier difference and Fourier syntheses. All the non-hydrogen atoms were refined anisotropically. All the hydrogen atoms were fixed by HFIX and placed in ideal positions. Calculations were performed using SHELXL 97,[54] SHELXS 97,[54] PLATON,[55] Olex2,[56] and WinGX system, version 1.80.05.[57]

2.4. Gas Chromatography and Catalysis. The catalytic studies were performed on small organic molecules (ethylbenzene, cyclohexanol, anthracene, benzyl alcohol, and cyclooctene) using **Comp1** and **Comp2** (5 mg). Detailed reaction conditions for each reaction were obtained from various literature procedures[32−34,42] and are provided in the Supporting Information. In a typical catalysis experiment, 5 mg of the finely powdered pure catalyst was taken in a 50 mL round-bottom (RB) flask on an oil bath, where the suitable solvents and reactants were added, and the reaction was done under constant stirring condition, between 70 and 90 °C and typical duration of 10−13 h. The products were analyzed by drawing 1 mL aliquots after reaction completion, using a Shimadzu GCMS-QP 2010 Plus gas chromatography instrument (coupled with a mass analyzer) to know quantitative amounts of products formed. The percentage conversion and selectivity were determined on the basis of the concentration of starting materials remaining after the reactions and the amount of various products formed at the end of the reaction. For catalyst recycling studies, the catalysts after the reactions were centrifuged, washed thoroughly with water and the corresponding organic solvent, dried overnight in a vacuum oven (at 70−80 °C), and then reused.

2.5. Dye Degradation Studies. Both the compounds were explored for photocatalytic dye degradation studies of methylene blue under UV light irradiation using a 250 W UV lamp. In a typical experiment, four different concentrations of aqueous methylene blue (MB) solutions were prepared in concentrations of the order of 1×10^{-5}. These four solutions were used to calibrate the absorbance (abs) versus conc curve for MB solution. With this calibration curve the concentration for any unknown MB solution could be directly determined from its absorbance value. An aliquot of 1×10^{-5} M (C_0), 50 mL of solution was taken for each measurement, and 10 mg of powdered catalyst was used. After addition of the catalyst, the solution was stirred in the dark for 1 h to reach the adsorption−desorption equilibrium. After that the UV light was put on, and 3 mL aliquots were taken at regular intervals of time for ~2 h. Then these aliquots were centrifuged (at 10 000 rpm for 15 min) immediately after drawing to get a clear supernatant, and concentration of dye remaining in the solution was determined through UV spectroscopic studies at the maximum wavelength of MB (665 nm). The degradation efficiency was calculated by the following formula.

$$\eta\ (\%) = \frac{C_o - C}{C_o} \times 100$$

where C_0 is the initial concentration of the dye, and C is the concentration at any given instant (t).

2.6. Electrochemical Studies. All the electrochemical measurements were performed at room temperature using a CHI 760E electrochemical workstation. Three-electrode setup was used consisting of glassy carbon (GC, diameter of 3 mm) as a working electrode, platinum wire as a counter electrode, and saturated calomel electrode (SCE) or Ag/AgCl as the reference electrode. The catalysts (**Comp1** and **2**) were mixed with 10 wt % Vulcan (2 mg of sample + 0.2 mg of Vulcan), and catalyst ink was prepared by adding 150 μL of H$_2$O and 50 μL of IPA with vigorous ultrasonication. Five microliters of this slurry was coated on a 3 mm diameter commercial glassy carbon electrode with addition of 2 μL of 0.1 wt % Nafion binder. The coated electrode was dried under air overnight before the electrochemical measurements. Before depositing the catalyst, the GC electrode was sequentially polished with 1, 0.3, and 0.05 mm alumina slurry and washed several times with distilled water. Cyclic voltammetry (CV) measurements were performed with 0.5 M H$_2$SO$_4$ aqueous solution at a scan rate of 50 mV s^{-1}. For the nitrite reduction studies, CV measurements were done using different KNO$_2$ (2.5 to 40 mM) concentration in 1 M aqueous (aq) H$_2$SO$_4$ solution at scan rates of 50 mV s^{-1}. Enhancement in the CV current values is indicative of the nitrite reduction properties of the catalysts. Pseudocapacitance studies were done in 0.5 M H$_2$SO$_4$ aqueous solutions through galvanostatic charge−discharge (GCD) measurements with different current densities (1−5 A/g) and cyclic voltammetry studies under varying scan rates (20−100 mV/s).

3. RESULTS AND DISCUSSIONS

3.1. Synthesis and Characterization. The compounds Na$_2$MoO$_4$·2H$_2$O(PMo)/Na$_2$WO$_4$·2H$_2$O(PW), Na$_2$HPO$_4$·2H$_2$O, CuCl$_2$·2H$_2$O, and 4,4'-bp were used to synthesize POMOFs by in situ hydrothermal method under identical synthetic conditions. We targeted the synthesis of two identical POMOFs with two different Keggin ions, to see their relative effects in the catalytic properties. Here the Keggin ions PMo$_{12}$O$_{40}$ and PW$_{12}$O$_{40}$ were synthesized in situ in a one-step reaction starting from the Mo and W oxides and disodium hydrogen phosphate (heteroatom source) through acid-catalyzed condensation reactions. The POMs acted as anionic ligands and formed the three-dimensional (3D) hybrid framework through interactions with the cationic Cu^{1+} metals ions coordinated with 4,4'-bp (1D chains). The Cu atom acts as nodal points joining Keggin ions with 4,4'-bp ligands. POMOF hybrid formation is one of the best ways to immobilize POM catalytic centers, whose high solubility in polar solvents greatly hinders their practical catalytic applications. The pH of the reactions proved to be very crucial for dimensionality and overall structure of the 3D hybrids, as it plays a crucial balance between the acidic pH required for the condensation of the POMs and the protonation of the N-coordinating sites of the 4,4'-bp. Interestingly it was observed that Cu^{2+} underwent a reduction to Cu^{1+} on incorporation into the POMOF structure. The presence of Cu^{1+} was evident from the magnetic properties (Figure S5), XPS (Figure 2a,b), and XANES (Figure 2c,d) measurements on both the compounds, which showed that the compounds are diamagnetic in nature at the room temperature, with Cu existing in its lower nonmagnetic +1 oxidation state. The in situ reduction of Cu^{2+} may have been induced by the reducing property of the ligand 4,4'-bp, where the N lone pairs reduced the Cu ion upon coordination, under the drastic reaction conditions of 180 °C, high pressure, and acidic environment. The syntheses were found to be extremely pH-sensitive, and slight variation of pH from the optimum values

led to the formation of impure or different phases. Many optimizations were done to fix the final pH of the reaction between 1.7 and 2.4. The 5 d hydrothermal reactions on cooling yielded hexagonal block/plate-shaped crystals in both the reactions with some secondary bluish-green Cu-bp impurities, which were washed away thoroughly with distilled water and acetone. The good-quality crystals were large (average dimension ~0.5 mm), dark red in color, and stable under aerial conditions as evident from the scanning electron microscopy (SEM) images (Figure S3). The insolubility of both the compounds in aqueous and organic solvents facilitated their use in heterogeneous catalytic applications. The compounds were obtained in good yields (~65−70% with respect to Na_2MoO_4/Na_2WO_4), and phase purity of the samples was analyzed through powder XRD measurements on the bulk samples (Figure 1). The powder XRD patterns of
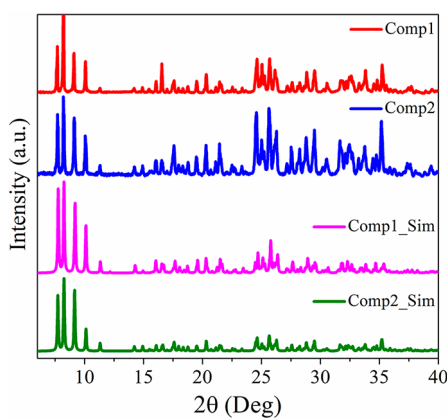

Figure 1. PXRD patterns of **Comp1** and **Comp2** compared with the simulated PXRD pattern of **Comp2** obtained from the SCXRD refinement.

Comp1 and **Comp2** confirmed the structural similarity of the twin hybrids crystallizing in the same space group ($P2_1/c$) with similar lattice parameters. The compounds were characterized by infrared spectroscopy (IR) and energy-dispersive X-ray spectroscopy (EDAX) to confirm the elemental compositions. IR clearly showed the presence of POMs $PMo_{12}O_{40}{}^{-3}$ and $PW_{12}O_{40}{}^{-3}$ in cases of **Comp1** and **2**, respectively (Figure S1). The peaks corresponding to the symmetric and asymmetric bond stretching modes for P−O, M═O_t, Mo−O_c−O, and Mo−O_c−P and that for P−O, W═O_t and W−O_b−W and W−O_c−P could be found in all the respective spectra below 1500 cm^{-1}. The peaks corresponding to the organic moiety arising from the 4,4′-bp were also present in the spectra, thus confirming the incorporation of the Keggin ions in the hybrid structure of **1** and **2**. The EDS spectra of both compounds confirmed both the qualitative and quantitative presence of each element in the hybrid structures. The atomic percentage ratios of the elements in both the compounds matched quite well with the elemental percentages obtained from the SCXRD data (Table S3) with acceptable deviations to confirm the structure determined through XRD.

Magnetic properties of the compounds were studied to understand the oxidation states of the metal atoms and overall magnetic state of the POMOF hybrids. Magnetic susceptibility studies were done between 2 and 300 K in the field-cooled mode at an applied magnetic field of 1000 and 100 Oe, respectively, on crystalline powdered samples of **Comp1** &

Comp2. There are two sources of origin of magnetism in each of the hybrids, which are Mo and Cu in **Comp1** and W & Cu in **Comp2**. Mo/W in the Keggin ions are expected to exist in their highest oxidation state of +6, in a d^0 nonmagnetic configuration. Cu during the synthetic stage was added as bivalent Cu^{2+} ion and hence could act as a magnetic center with one unpaired electron. The temperature-dependent magnetic susceptibility (χ_M) data for **Comp1** & **2**, shown in Figure S5a,c respectively, however, clearly indicate that both the compounds are diamagnetic in nature in the room-temperature regime. The χ_M values are negative (**Comp1**) or very close to 0 (**Comp2**) in the entire temperature range of 200−300 K. Field-dependent magnetization studies were performed at 2 and 300 K (Figure S5b,d) for both the compounds. The negative slope of the linear dependence of the magnetic moment with the varying magnetic field (*M* vs *H*) at 300 K clearly shows that the systems are of diamagnetic nature at room temperature. Thus, it indirectly proves that the Cu ions in both the hybrids exist in their nonmagnetic +1 oxidation state along with the Mo/W existing in their stable +6 oxidation state. *M* versus *H* data at 2 K, however, shows a typical sigmoidal behavior, with magnetic moment value saturating at higher fields, which is indicative of the presence of a small amount of paramagnetism in the system. This behavior could be associated with slight paramagnetic oxygen crystallized at low temperature and saturation of magnetic vacancies in the partially occupied atomic positions.[32] Thus, from the susceptibility and magnetization data it is evident that there has occurred a reduction in the Cu ion during the progress of the reaction from its pristine +2 to the existing +1 state. To further confirm the oxidation states of the Mo and the Cu atoms in the POMOF structure, room-temperature XPS measurements were done on **Comp1**, at the Mo 3d and Cu 2p regions. The Mo 3d region (210−240 eV) and the Cu 2p region (920−960 eV) were fitted to get well-separated peaks for Mo 3d5/2 (231.6 eV) and 3d3/2 (234.7 eV) and Cu 2p3/2 (932.5 eV) and 2p1/2 (953 eV) (Figure 2a,b). The binding energy values and full width at half-maximum (fwhm) of the peaks are well in agreement with reported data for Mo 3d and Cu 2p electrons.[58,59] The binding energies indicate that the Mo and Cu in **Comp1** are in +6 and +1 oxidation states, respectively. Since the Cu ion electronic state and geometry are crucial to the hybrid structure, and their catalytic and optical properties, the oxidation state of the Cu centers were further analyzed through XANES measurements. The XANES spectra obtained at the Cu edge for **Comp1** and **Comp2** (Figure 2c,d) clearly indicate the existence of +1 oxidation state of Cu as evident from the shoulder peak corresponding to the 1s → 4p$_z$ transition.[60] Thus, from the combined magnetic, XPS, and XANES studies we could clearly identify the oxidation states of the metal ions in both the hybrid POMOFs, and the general magnetic properties of the compounds were elucidated.

3.2. Crystal Structure. Both the compounds **Comp1** and **Comp2** crystallize in the monoclinic crystal system with space group $P2_1/c$ and similar lattice parameters of *a* = 11.5114 (2) Å, *b* = 22.7519(5) Å, *c* = 11.4144(2) Å, β = 111.556°(10), *V* = 2742 (10) Å^3 and *a* = 11.4797(2) Å, *b* = 22.8418(5) Å, *c* = 11.4225(2) Å, β = 111.217°(10), *V* = 2792 (10) Å^3, respectively. Both the compounds crystallize with similar molecular arrangements with slightly varied cell origin and position of symmetry elements, which has been elaborated in the later part of this section. The crystallographic data and
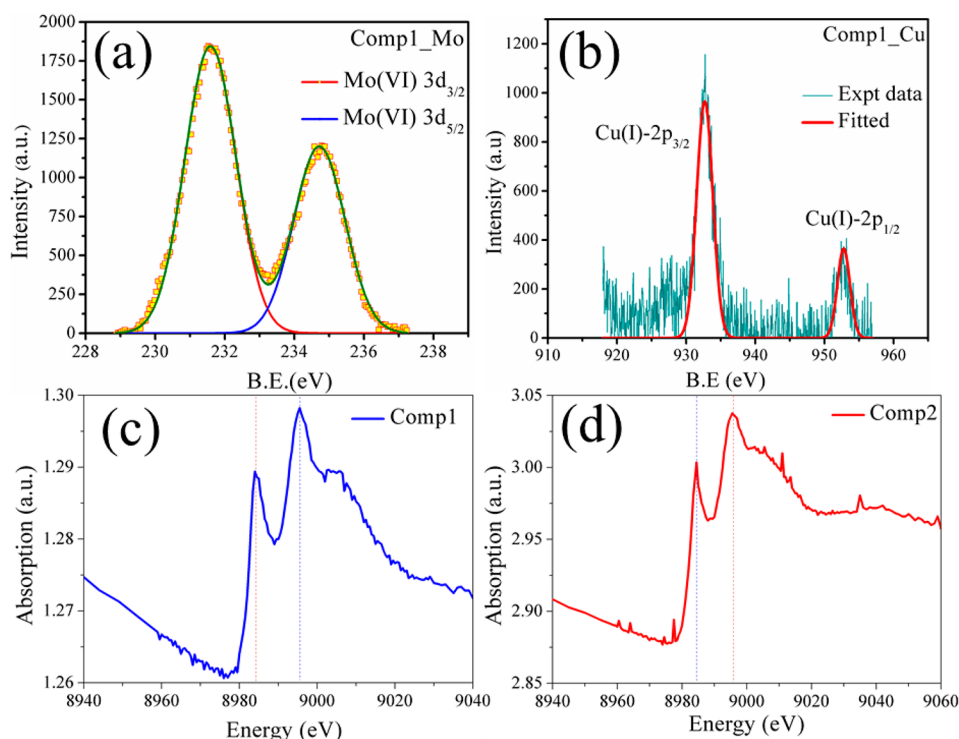
Figure 2. Spectroscopic analyses of **Comp1** & **Comp2**: (a) XPS spectra of Mo energy of Comp1, (b) XPS spectra at Cu energy of **Comp1**, XANES spectra at Cu edge of (c) **Comp1** and (d) **Comp2**.

**Table 1. Crystal Data and Structure Refinement for Comp1 at 100 K and Comp2 at 298 K**

	Comp1	Comp2
empirical formula	$C_{30}H_{24}N_6Cu_2Mo_{12}O_{40}P$	$C_{30}H_{24}N_6Cu_2W_{12}O_{40}P$
formula weight	2417.88	3472.80
temperature	100.0 K	298.0 K
wavelength	0.710 73 Å	
crystal system	monoclinic	
space group	$P2_1/c$	
unit cell dimensions	$a = 11.5172(2)$ Å, $b = 22.6508(5)$ Å, $c = 11.3008(2)$ Å, $\beta = 111.5210(10)°$	$a = 11.4797(2)$ Å, $b = 22.8418(5)$ Å, $c = 11.4225(2)$ Å, $\beta = 111.2170(10)°$
volume	2742.55(9) Å^3	2792.15(9) Å^3
Z	2	
density (calculated)	2.928 g/cm^3	4.131 g/cm^3
absorption coefficient	3.540 mm^{-1}	25.482 mm^{-1}
F(000)	2286	3054
crystal size	$0.1 \times 0.08 \times 0.04$ mm^3	$0.09 \times 0.06 \times 0.02$ mm^3
θ range for data collection	2.643 to 25.998°	3.714 to 25.999°
index ranges	$-13 \leq h \leq 14$, $-27 \leq k \leq 17$, $-13 \leq l \leq 13$	$-14 \leq h \leq 13$, $-28 \leq k \leq 26$, $-12 \leq l \leq 14$
reflections collected	23 763	23 696
independent reflections	5366 [$R_{int} = 0.0338$]	5452 [$R_{int} = 0.0657$]
completeness to $\theta = 25.998°$	99.5%	99.4%
refinement method	full-matrix least-squares on F^2	full-matrix least-squares on F^2
data/restraints/ parameters	5366/30/460	5452/54/437
goodness-of-fit	1.011	1.019
final R indices^a [$I > 2\sigma(I)$]	$R_{obs} = 0.0393$, $wR_{obs} = 0.0887$	$R_{obs} = 0.0347$, $wR_{obs} = 0.0798$
R indices^a [all data]	$R_{all} = 0.0454$, $wR_{all} = 0.0941$	$R_{all} = 0.0465$, $wR_{all} = 0.0867$
largest diff peak and hole	2.015 and -1.541 e·Å^{-3}	1.556 and -1.645 e·Å^{-3}

$^aR = \sum||F_o| - |F_c||/\sum|F_o|$, $wR = \{\sum[w(|F_o|^2 - |F_c|^2)^2]/\sum[w(|F_o|^4)]\}^{1/2}$, and $w = 1/[\sigma^2(F_o^2) + (0.0271P)^2 + 35.0168P]$ for **Comp1** & $w = 1/[\sigma^2(F_o^2) + (0.0337P)^2 + 17.4790P]$ for **Comp2**, where $P = (F_o^2 + 2F_c^2)/3$.

refinement details are provided in Table 1. Because of the presence of the bigger atom W (instead of Mo) in **Comp2**, the

lattice parameters and cell volume of **Comp2** are slightly higher than those of **Comp1**. The molecular formulas of
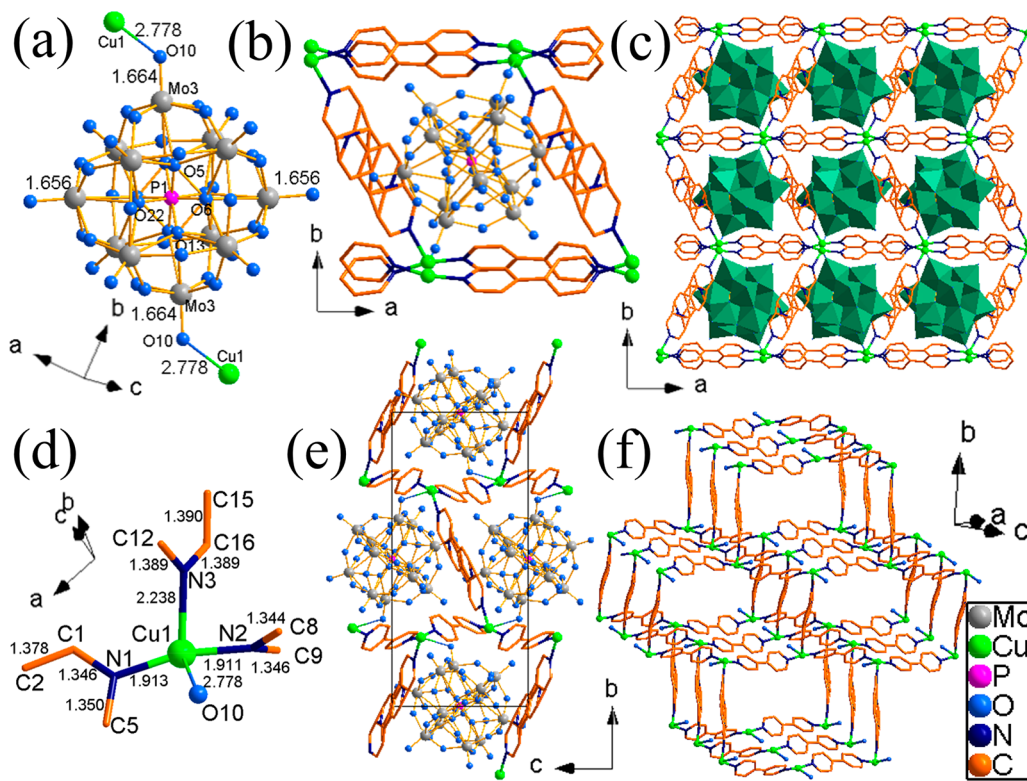
Figure 3. Crystal structure of **Comp1**: (a) POM unit, (b) molecular structure, (c) 3D arrangement along *c*, (d) coordination environment of Cu, (e) unit cell structure, and (f) bp arrangement.
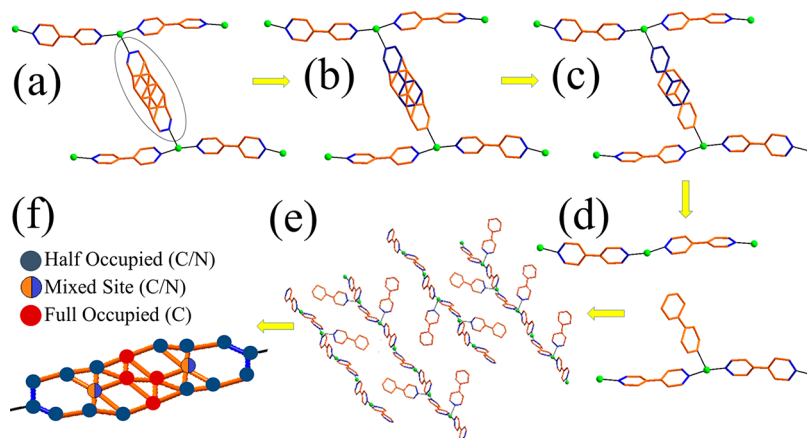

Figure 4. Resolving the structure of disordered bipyridine ring.

Comp1, $[H(C_{10}H_{10}N_2)Cu_2][PMo_{12}O_{40}]$, and **Comp2**, $[H-(C_{10}H_{10}N_2)Cu_2][PW_{12}O_{40}]$, are analogous with the difference in addenda atom of the POM unit. The molecular structure of **Comp1** & **Comp2** consists of the one 4,4′-bp unit, two Cu ions, and one Keggin POM unit (Figures S6 and S7). The unit cell structure (Figure 3e) of **Comp1** reveals that the central P atom of the POM unit sits at the face centers of four of the faces in the unit cell. The POM units in both the hybrids are having the usual disorder at the core oxygens, where eight half-occupied oxygen atoms coordinate the central Si atom in superimposing tetrahedral geometry, which appears as an average cuboctahedral coordination environment.[18] The disordered 4,4′-bp unit passes through the vertices and the two remaining face centers of the unit cell. The 2D hybrid structures in both **Comp1** are built through 1D Cu-bp chains

progressing along the *ac* direction, which are coordinated by the POM units along the *ab* direction to form a 2D arrangement with Cu acting as the nodal points of coordination. Such layers are interconnected with parallel units through hydrogen-bonding interactions between two adjacent POMs, through the terminal oxygens (O20−O14:2.93 Å), and also between the terminal oxygen of the POMs with the nitrogen of 4,4′-bp of a parallel or adjacent 1D chain or POM-1D-chain layer. Clearly the secondary structures are completely built through supramolecular interactions origination from the Keggin ion. The progress of the 1D chains is very interesting, which is slightly puckered in nature. The nodal Cu (Cu1) ion in the 1D chain is tetrahedrally (slightly distorted) coordinated (Figure 3d), with two nitrogens (N1, N2) of two coordinating 4,4′-bps on either
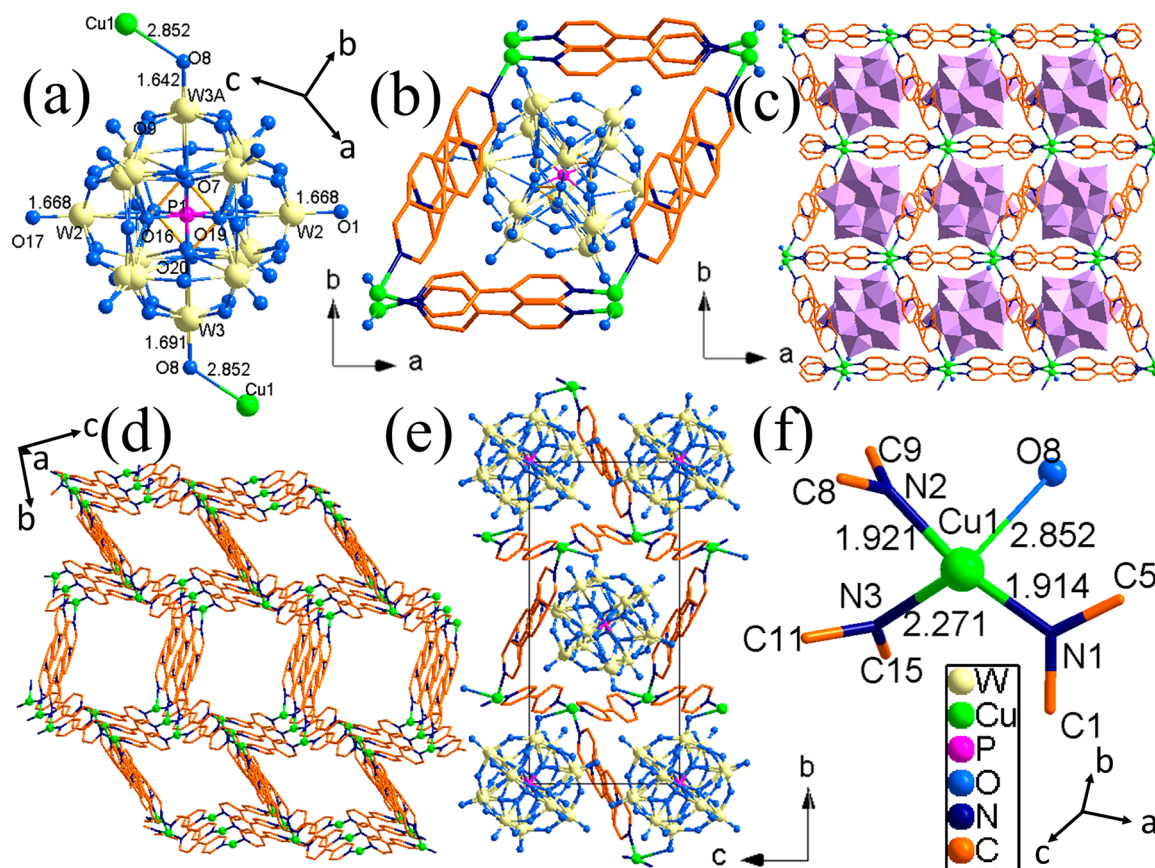
Figure 5. Crystal structure of **Comp2**: (a) POM unit, (b) molecular structure, (c) 3D arrangement along c, (d) bp arrangement, (e) unit cell structure, and (f) coordination environment of Cu.

side, another nitrogen (N3) of a third 4,4′-bp oriented at 90° to the 1D chain and the terminal oxygen (O10) of the POM unit. The bond distances of Cu−N (1.91 Å for N1 & N2, 2.238 Å for N3) and Cu−O (Cu−O10: 2.778 Å) are within acceptable ranges, though it is evident that the bonds with the POM-oxygen or the secondary bp are much weaker as compared to the interactions with the bp-nitrogen atoms along the chain. Along the 1D chain, every adjacent Cu atom has an alternate arrangement of the secondary bp (N3) and the coordinating POM (O10), where the relative orientation of the N3 and the O10 flips by 90°(Figures 3, 4, S8). If two parallel 1D Cu-bp chains are considered, it can be observed that each alternate Cu center has a coordinating lone 4,4′-bp perpendicular to the direction of the 1D chain, which projects out between the chains (Figures 3 and S6). When X-ray averages out the crystallographic image of two 4,4′-bps coming from the opposite direction of the two parallel Cu-bp chains, the superimposed structure gives rise to a heavily distorted 4,4′-bp unit, which has been resolved in Figures 4 and S8. The most complicating part of solving the disorder was location of the symmetry element "i" at the center of the disordered ring, which symmetry generated one-half of disorder ring. Now, since the occupancies of the atoms were very different along the various positions on the disordered ring, it was very critical to resolve the disorder out of the symmetry operation in the structure. As shown in Figure 4f, the disordered unit consists of two opposing 4,4′-bp rings of parallel 1D chains, where six atoms are common between the rings, four of which (at the center) are fully occupied C atom positions (half occupancy from each ring), two fully occupied mixed sites having half

occupancy each for C and N of the two opposing rings. All the remaining 14 atoms are half occupied, with two of them being nitrogen atoms (coordinated to the Cu in each of the parallel 1D chains) and the remaining 12 being half-occupied carbons (six from each bp unit). This 4,4′-bp ring coordinated to the Cu node as the fourth arm of the tetrahedra is actually instrumental in stabilizing the interchain and interlayer interactions through hydrogen bonding (O21$_{POM}$−N3$_{bp}$: 2.97 Å) and electrostatic interactions with the POM unit and CH-π (2.7−2.8 Å) interaction with the 4,4′-bp of the 1D chain. Thus, the overall 3D structure is composed of both covalent (Cu-bp, Cu-POM) and noncovalent (H-bond$_{POM−POM}$, H-bond$_{POM-bp}$, CH-π_{bp-bp}) interactions between the Cu cations, 4,4′-bp units, and the anionic Keggin ion, where the POM units direct and template the overall POMOF structure.

Structural arrangement of compound **Comp2** is similar to that of compound **Comp1** as evident from the similar lattice parameters. The molecular arrangement of the **Comp2**, as in **Comp1**, is composed of the disordered Keggin ion **PW$_{12}$O$_{40}$**, the coordinated 1D-Cu-bp chains, and the disordered 4,4′-bp units. The POM structure, molecular unit, unit cell structure, 3D arrangements, and the orientation of the bp chains are shown in Figure 5. There are slight differences in the lattice parameters and the cell volume arising from the bigger W addenda atom of the Keggin ion. The major difference between the two structures lies in the unit cell arrangements where, in the case of **Comp2**, the POM center (P atom) occupies two of the face centers and the vertices of the unit cell, while the remaining four face centers are occupied by the disordered 4,4′-bp ring. The 3D structural arrangement

Table 2. Results of Blank and Catalytic Reaction (Conversion and Selectivity) of Different Small Molecule Oxidation of Comp1 and Comp2

| code	reaction name	constituents		conditions	conversion (%)			selectivity (%)		
		reagents	amount		blank	1	2	blank	1	2
C1	oxidation of ethylbenzene	ethylbenzene	0.3 mL (2.4 mmol)	12 h, 70 °C	30	72	69	43	acetophenone (72)	acetophenone (94)
		acetonitrile	8 mL							
		70% TBHP	0.745 mL (4.8 mmol)							
C3	oxidation of anthracene	anthracene	0.05 g	12 h, 75 °C	20	31	82	50	anthraquinone (100)	anthraquinone (93)
		70% TBHP	0.125g							
		benzene	5 mL							
C5	epoxidation of cyclo-octene	cyclo-octene	1 g (10 mmol)	10 h, 85 °C	negligible	74	40		cyclo-octene epoxide (80)	cyclo-octene epoxide (62)
		TBHP	0.136 g (4 mmol)							
		1,4-dioxane	10 mL							

consists of the 1D Cu-bp chains, which progress along the *ac* direction and are connected with each other along the *ab* direction through anionic POM units. Such 2D layers are interconnected by interactions between the two adjacent POM units (O17−O21) and POM and 4,4′-bp units of the 1D chains (O8−H5, O8−H9, O1−C1). The Cu geometry is almost identical to that in **1**, with slight changes in bond angles and distance. The Cu atom (Cu1) is tetrahedrally coordinated by two nitrogen atoms of the coordinating 4,4′-bp chains (N1: 1.91 Å, N2: 1.92 Å), one nitrogen of the disordered 4,4′-bp unit (N3: 2.27 Å), and terminal oxygen of the POM unit (O8: 2.85 Å). The overall structural organization and the nature of the lone 4,4′-bp disorder is completely similar to that in **Comp1**, where covalent interactions between the Cu-bp and Cu-POM units and noncovalent interactions like H-boding and electrostatic between two POMs, POM & the disordered 4,4′-bp, POM & the 1D-chain-bp, and CH-π interactions between the disordered 4,4′-bp unit and the 1D-chain-bp stabilize the 3D structure in the POMOF hybrid.

3.3. Heterogeneous Catalytic Studies. POMs, particularly the Keggin ions, are generally known to show good catalytic properties toward selective oxidation of small organic molecules.[6,61] Here we chose to study the catalytic property of the hybrid POMOFs for a set of five peroxide-mediated catalytic oxidation reactions of (1) benzyl alcohol, (2) ethylbenzene, (3) anthracene, (4) cyclohexanol, and (5) epoxidation of cyclo-octene. The detailed reaction conditions are provided in the Supporting Information which mostly followed one of our previous reports.[32] All catalysis studies were done using finely powdered single crystals (phase purity checked) of **Comp1** and **Comp2**. Before the catalytic studies, to check the stabilities of POMOFs in reaction media, powdered catalysts were treated with various organic solvents, used in the catalysis, overnight at a temperature of 70 °C. Post-treatment PXRD analyses (Figure S9) of the samples and elemental analyses of the supernatant proved that the hybrids are very stable under the catalytic conditions in the polar/nonpolar organic media. The high chemical stability of the POMOFs in a wide range of organic solvents allowed us to screen various oxidative catalysis studies using varying reaction conditions. The results of the catalytic studies with the conversion, selectivity, and product yields (with catalyst and blank) are shown in Tables 2, S4, and S5 and Figure 6. Two sets of blank reactions were conducted, one at 25 °C (without temperature), and the other without the catalysts. Conversion
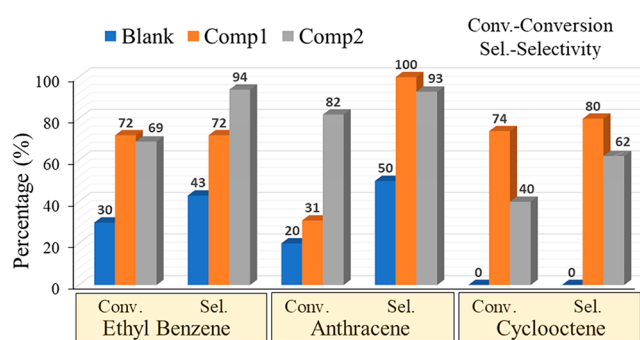
Figure 6. Comparison of the percentage conversion and selectivity of blank and catalyzed (**Comp1** & **Comp2**) oxidation of small organic molecules.

results clearly indicated that both temperature and catalyst are needed for the successful partial oxidation for the reactants. As there was negligible conversions for the reactions at 25 °C, all the reactions were conducted at the corresponding temperatures between 70 and 90 °C, as mentioned in the Supporting Information and Tables 2 and S4. From the comparison of the reaction outputs with and without catalysts it is clear that both the catalysts are highly active for oxidation of small organic molecules. Both the compounds were found to be very less active for the oxidation of cyclohexanol and that of benzyl alcohol with negligible yield. In case of the epoxidation of cyclooctene for compound **1** there was a drastic increase in activity on altering the catalytic solvent from acetonitrile to 1,4-dioxane. Both the compounds **Comp1** & **Comp2** were found to be highly active and selective catalysts for oxidation of ethylbenzene, anthracene, and cyclooctene with 2−3 times enhancement in conversion and selectivity as compared to the blank reactions. **Comp1** oxidized ethylbenzene to acetophenone with a conversion efficiency and selectivity of 72% each. For the oxidation of anthracene to anthraquinone, **Comp1** showed 100% selectivity for the desired product with a conversion efficiency of 31%, which is 10% higher than that of the blank reaction. On the one hand, **Comp1** particularly showed excellent activity for the epoxidation of cyclooctene, where **1** exhibited a conversion efficiency of 74% with a selectivity of 80% for cyclooctene-epoxide, as compared to negligible or no conversion for the blank reaction. **Comp2**, on the other hand, was most active for the catalytic oxidation of anthracene, where it showed a conversion efficiency of 82% (4
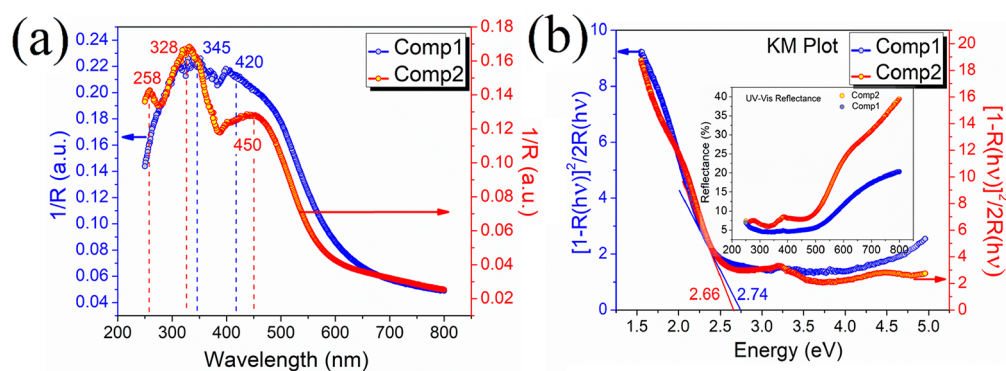
Figure 7. (a) UV−Vis spectroscopy studies and (b) Kubelka−Munk function plots of **Comp1** & **Comp2**. (inset, b) Reflectance spectra of the hybrids.

times higher than the blank reaction) with a high selectivity of 93% for anthraquinone. It showed a similar conversion to **Comp1** for ethylbenzene oxidation with 69% conversion but much higher selectivity of 93% for acetophenone. The catalytic activity of **Comp2** for cyclooctene conversion, however, was lower than that of **Comp1**. The overall catalytic studies evinced that both the hybrid POMFs are good stable catalysts for oxidation of small molecules, with good conversion and excellent selectivity. The stability and the recyclability of the catalysts were studied over three catalytic cycles, where the catalysts after each reaction were separated by centrifugation, thoroughly washed with distilled water and corresponding organic solvents, and dried overnight in vacuum oven (70−80 °C) before reuse. Recycling catalytic activity and leaching tests proved that the catalysts are stable and recyclable with marginal variation in activity (0−3%). Slight poisoning of the catalytic active sites by organic substrates may have led to little variation in the activity in the recycling tests. On a comparative analysis, it could be concluded that **Comp2** is a better oxidation catalyst than **Comp1**, though the relative variations in the activity were not major and lay within the range of 10−20% in terms of conversion and selectivity. The structural and electronic characterizations proved that the catalysts are completely identical in terms of 3D architecture, pore size distribution, surface area, and electronic/oxidation states of the Cu and Mo/W metal ions. Thus, the only probable factor playing a role in the catalytic activity was the nature of the Keggin ion and their relative acidities. It could be concluded for the oxidation of ethylbenzene and anthracene catalytic activity increase with increasing acidity of the POM unit, while the reverse order was followed for cyclooctene epoxidation.[35] The catalytic mechanisms of peroxide-mediated oxidations involving POMs are very well-studied in case of homogeneous catalysis, where the peroxide reacts with POM units to generate the catalytic reactive species (Ishii−Venturello complex),[33] which acts as the active catalyst for oxidation. In heterogeneous catalysis, the mechanisms are comparatively less explored, which may vary across different reactions and different natures of hybridization used.[62] Heterogeneous catalytic mechanism can however be decoupled to two steps of activity, (1) substrate activation and (2) reactive oxygen species formation. Since in heterogeneous catalysis, direct interaction of peroxides with the POM units by breaking of the clusters is less likely to occur, it may be expected that the redox activity and oxygen insertion processes are decoupled through the POM unit and peroxide species, respectively, where the organic units may play the crucial role of substrate adsorption/

activation, guiding the pathways and kinetics of the overall reaction. In such a scenario, though synergistic interactions between the peroxide, POM and organic subunits are expected, direct oxygenation of substrates through reactive/modulated POM-peroxide species is very less likely. The pores, dimensionality, and structural hierarchy of the hybrid structure is expected to play a crucial role in activation and interaction pathway of the substrates with the catalytically active sites. As evident from various reports on homogeneous catalysis using POMs for similar reactions, it can be concluded that it is difficult for POMOF (heterogeneous catalysts) to beat their activities, which usually exhibit conversion values in the range of 85−95%. However, on comparison with different POM-hybrids exploited in similar heterogeneous catalytic application, it can be clearly seen that both the compounds have comparable or in some cases much better activity for partial small molecule oxidation. Table S6 shows a comparison of data for catalytic oxidation of previously reported POM-based catalysts (homogeneous and heterogeneous) with this report, which signifies the rich catalytic properties of the POMOFs reported here. However, it must be mentioned that direct comparisons with other catalyst should be done with careful considerations as the reactions conditions like temperature, solvents, oxidative reagents, and particularly reaction durations are widely different among various cases.

3.4. UV−Vis Spectroscopy and Optical Band Gap. The compounds were reddish-orange in color indicating that they have visible light absorption and suitable band gap. This prompted us to study the UV−vis absorption and optical band gap studies of these compounds. The electronic spectra of **Comp1** & **Comp2** were recorded on phase-purity-checked finely powdered single crystals of both in solid medium in the reflectance mode in the range of 200−800 nm. Diffuse reflectance spectroscopy (DRS) was used to plot the Kubelka−Munk function, where the reverse extension point between energy axis and linear Kubelka−Munk absorption intensity was used to determine the optical band gap of the compounds (Figure 7).[63] As expected from the color of the compounds the band gaps were obtained to be 2.74 and 2.66 eV for **Comp1** & **Comp2**, respectively (Figure 7b). The band gap indicates that the compounds are semiconducting in nature, which is a clear transition from the individual precursor units (4,4′-bp and POMs), which are well-known insulators. **Comp1** & **Compd2** in the solid UV spectra showed bands in both UV and visible regions. **Comp1** showed two absorption peaks at 345 and 420 nm, which can be attributed to the ligand-to-metal charge transfer (LMCT) and n−π*/π−π* transitions of the 4,4′-bp
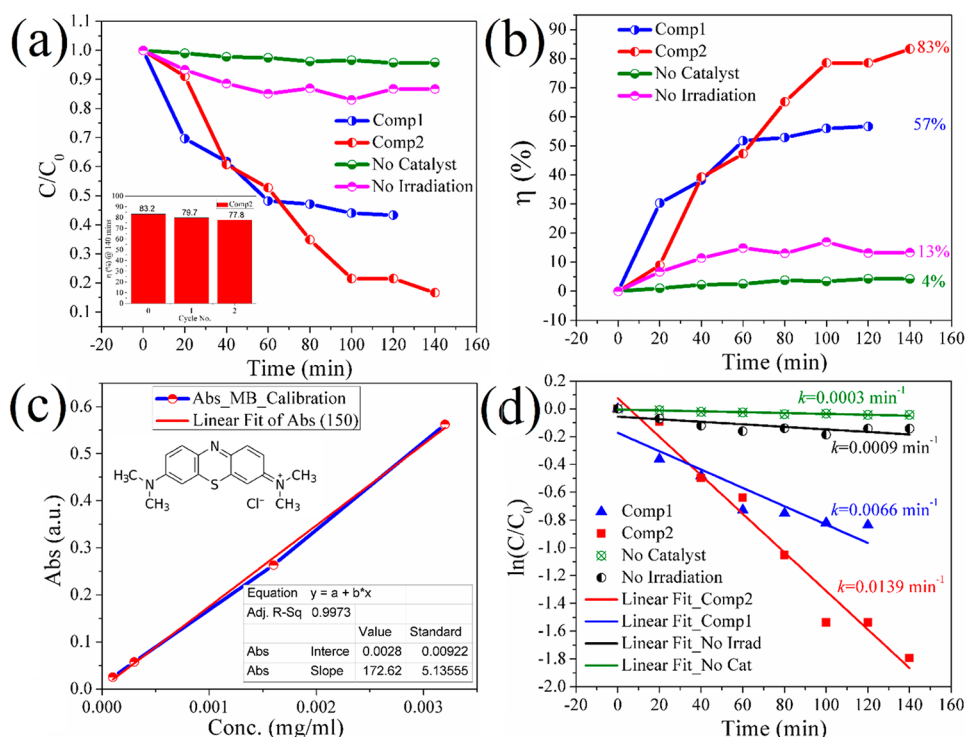
Figure 8. Photocatalytic dye degradation study of **Comp1**, **Comp2** & controls: (a) conc decay vs time, (b) efficiency vs time, (c) calibration curve for MB, (d) rate constants for **Comp1** & **Comp2** and controlled studies.

ligand.[64] **Comp2** shows three absorption bands 258 nm, 328 nm and 450 (Figure 7a). The first band, which is visible as a slight shoulder in case of **Comp1**, can be associated with the oxygen(O)−tungsten(W-addenda) charge-transfer absorption band for Keggin anions.[65] The remaining two bands can be attributed to the LMCT and n−π^*/π−π^* transitions of the 4,4′-bp ligand.[64] Thus, from the UV−vis spectroscopic studies it was evident that both the compounds have the potential to show photocatalytic properties, which are discussed in the next section.

3.5. Photocatalysis. Organic dyes are a class of very harmful chemical pollutants that are the eliminated by many industries (textile, printing), which contaminate groundwater if the effluent is not treated properly before discharge. Thus, developing catalysts that can degrade these dyes under light irradiation is of considerable importance. To explore the photocatalytic dye degradation properties of the catalysts (**Comp1** & **Comp2**), methylene blue (MB) was chosen as a representative dye, and photocatalytic studies were performed under UV irradiation (250 W). In a typical experiment four different concentrations on the order of 1×10^{-5} of aqueous MB solutions (0.0032, 0.0016, 0.0003, 0.0001 mg/mL) were prepared as standards to derive calibration curve (Abs vs Conc, Table S7, Figure 8) for the MB solution. The degradation studies were studied by directly measuring the absorbance at the absorption maxima (665 nm) of the MB dye. As evident from Figure 8, the photocatalytic degradation efficiency, denoted as $(1 - C/C_0) \times 100$, increased from 4% (without catalysts) and 13% (without irradiation) to 57% for **Comp1** and 83% for **Comp2**, in 120 and 140 min of irradiation, respectively, signifying the photoactivity of the twin catalysts. The activity of the catalysts was found to saturate after 140 min, probably due to lack of further electron acceptors. The compounds showed comparable/better activities, at lesser

irradiation time (120 min), than some of the reported POMs-hybrids, like that of Keggin-, Dawson-, and P_4Mo_6-based hybrids, which showed 63%, 94%, and 96.52% of MB degradation, respectively, after 180 min.[66,67] **Comp2** showed better photocatalytic activity (83% to 57% degradation efficiency) than **Comp1**, which may be because of the slightly higher surface area of **Comp2**, facilitating higher substrate interactions and better UV-absorption efficiency of **2** over **1** as evident from the prominence of the POM charge transfer band at 258 nm in case of **Comp2**. The photoredox activity of $PW_{12}O_{40}$ unit is known to be richer than that of $PMo_{12}O_{40}$, which was reflected in the photocatalytic activity of the two hybrids. The initial concentrations of dyes after the adsorption−desorption equilibrium were slightly different between **Comp1** (0.0007 mg/mL) and **Comp2** (0.0013 mg/mL). **Comp2** at the end of 140 min yielded a dye concentration of 0.0003 mg/mL (Table S7). The dynamic degradation and decomposition plots are shown in Table S7 and Figure S10. POMs in these kinds of hybrids are expected to potentially play twin roles, one being the active catalytic site itself, and the second being the potential electron acceptor to decouple the electron hole pairs in the photoinduced charged state of the hybrid.[68] To understand the kinetics and apparent rate constants (k, min^{-1}) of the pseudo-first-order reaction, $\ln(C/C_0)$ was fitted against time (t, min), where C_0 and C are the initial and instantaneous MB concentrations along the irradiation time gradient. The rate constants for **Comp1** and **Comp2** were found to be 0.0066 min^{-1} and 0.0139 min^{-1}, respectively (Figure S10, Table S7), while those for the controlled studies were very low, 0.0009 min^{-1} (no irradiation) and 0.0003 min^{-1} (no catalyst). Interestingly, the rate constant for **Comp2** ($k = 0.0139$ min^{-1}, $k_2 = 0.79 \times k_{P25}$) is comparable to that of the well-known catalyst P25 ($k = 0.0177$ min^{-1}).[68] To check the recyclability of the catalysts, **Comp2** was reused
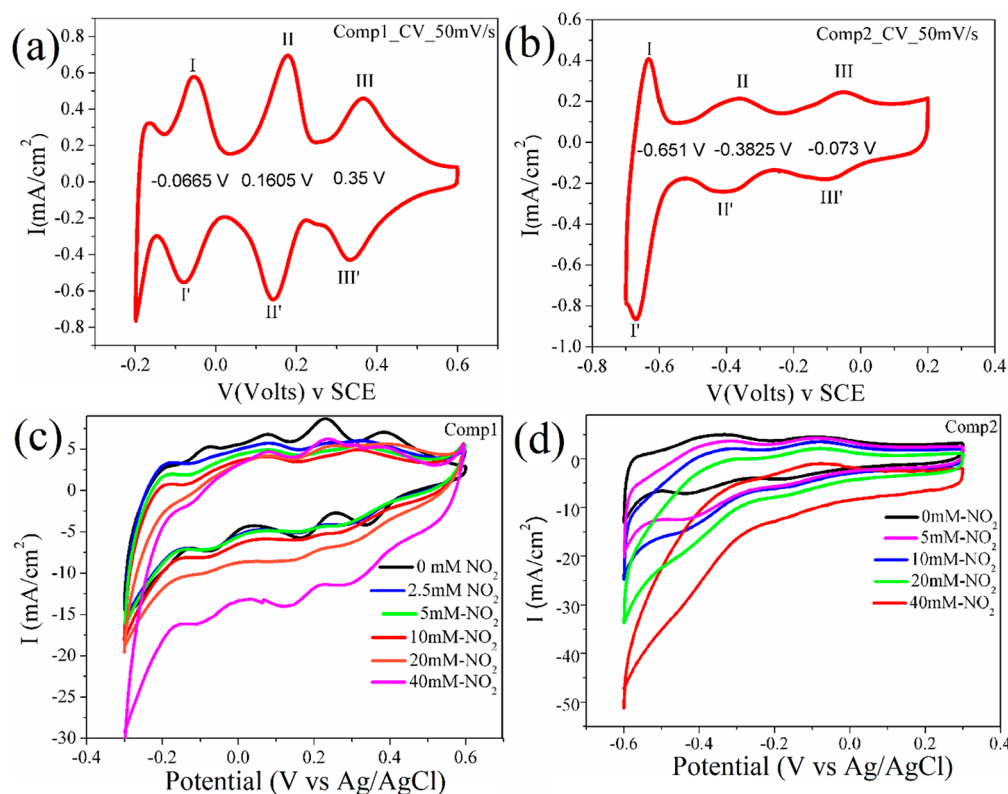
Figure 9. Electrochemical properties of **Comp1**, **Comp2**: (a) CV of **1**, (b) CV of **2**, CVs for nitrite reduction studies of (c) **Comp1** and (d) **Comp2**.

after thorough washing (ultrasonication), drying, and heat treatment for activation for three cycle testing. As evident from the inset of Figure 8a and Figure S10, there was slight decrease in activity of compound in terms of efficiency after 140 min (83% to 77.8%), which is usual and is often attributed to the loss of catalyst during regeneration treatment. Since considerable changes in activity were not observed, it could be concluded that the catalyst was stable under photoirradiation in the catalytic media, which makes **Comp2** a very good catalyst for photodegradation of harmful dyes like MB.

3.6. Electrochemical Properties. The electrochemical properties of the two POMOF hybrids were studied in 0.5 or 1 M aq H_2SO_4 solutions, as and where mentioned. The reversible CV redox peaks ($E_{1/2} = (E_{pa} + E_{pc})/2$) for **Comp1** (−0.0665, 0.1605, 0.35 V vs SCE) and for **Comp2** (−0.651, −0.3825, −0.073 V vs SCE) can be seen in the cyclic voltammetry curves in Figure 9a,b, respectively, corresponding to the different one- and two-electron processes of W and Mo centers, which is expected at acidic pH conditions with subsequent protonation during the two-electron reduction steps.[11,28] The electron reduction pathways in the Keggin ions are dependent on the pH, where $PW_{12}O_{40}{}^{3-}$ is expected to show two one-electron reduction and one two-electron process, all of which are reversible, while the Mo is expected to undergo five reversible two-electron reductions. The CV current variation with scan rates is depicted in Figure S11. The peak potentials vary marginally on gradual variation of the scan rates from 5 to 100 mV·s^{-1}, with average peak potentials remaining constant. The proportionality of the peak currents with the scan rates signifies that the redox processes for **Comp1** & **Comp2** are surface-controlled.[28] POMs are well-known catalysts for electrocatalytic nitrite reduction.[69−72] We investigated the nitrite reduction properties of **Comp1** and **Comp2**. As evident from Figure 9c,d, it can be concluded that the reduction peak currents of both the compounds increase with the increase in nitrite concentration from 2.5 to 40 mM, along with the decrease in anodic peak currents, suggesting that both the compounds show good electrocatalytic activity for reduction of nitrite.

Pseudocapacitance. Pseudocapacitance mainly occurs due to the faradaic charge transfer process.[73,74] The main difference between batteries and pseudocapacitors is in the time taken for the completion of the charge−discharge cycles, which in pseudocapacitors is typically on the order of minutes or seconds. The pseudocapacitance measurements were done using CV and galvanostatic charge−discharge (GCD) techniques. These studies were performed in a three-electrode setup using saturated calomel electrode as the reference, Pt coil as counter, and glassy carbon as the working electrode. The formula for calculating the specific capacitance C_s from GCD is
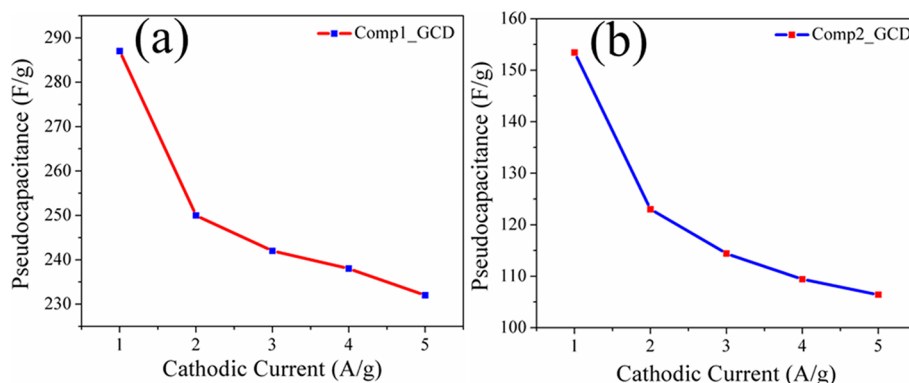
$$C_s = \frac{I\Delta t}{m\Delta V}$$

where I = current applied (A), Δt = discharge time (sec), m = catalyst mass (g), and Δt = potential window of the reaction (V).

Specific capacitance from CV can be determined by the following formula

$$C_s = \frac{\int_{V_i}^{V_f} I \, dv}{(V_f - V_i)m \, (dv/dt)}$$

Figure 10. Electrochemical pseudocapacitance studies of **Comp1** & **Comp2**: Specific capacitance vs current density plots of (a) **Comp1** and (b) **Comp2**.

where I = current under the area of CV curve (A), (Vf,Vi) = potential window (V), m = catalyst loading (g), dv/dt = scan rate (mV/Sec).

The GCD plots for **Comp1** were recorded at different current densities ranging from 1 to 5 A/g, and the voltage window used was 0.6 V (Figure S12). The specific capacitance values (C_s) are 287, 250, 242, 238, and 232 F/g, respectively, at 1, 2, 3, 4, 5 A/g (Figure 10a, Table 3). The C_s after 500

Table 3. Specific Capacitances of Comp1 & Comp2 from GCD and CV Studies in 0.5M H_2SO_4

current densities (A/g)	CV scan rates (mV·s^{-1})	specific capacitance			
		Comp1		Comp2	
		GCD (F/g)	CV (F/g)	GCD (F/g)	CV (F/g)
1	20	287	452	153.43	395
2	30	250	453	123	360
3	50	242	450	114.4	363
4	75	238	447	109.4	367
5	100	232	447	106.4	370

cycles is measured at a current density of 1 and 3 A/g, for which **Comp1** shows an activity of 53 F/g for both the current densities. The GCD curves of 1 and 3 A/g show 81.5% and 78.14% of degradation in the activity. The CV curves were recorded between 0 and 0.6 V at scan rates ranging from 20, 30, 50, 75, to 100 mV, and the specific capacitance values calculated were 452, 453, 450, 447, and 447 F/g, respectively. The CV plots after the 500 cycles ADT shows a rectangular nature indicating the presence of electrochemical double layer capacitance (EDLC) behavior. The sample's CV was collected at 50 mV and 100 mV/s scan rate after ADT, and the C_s values obtained were 127.3 and 122 F/g (Figure S12). The CV curves show a 71.7 and 72.7% degradation in the specific capacitance at 50 mV and 100 mV/s, respectively.

The GCD plots for **Comp2** were recorded at current densities ranging from 1 to 5 A/g at a different voltage window of 0.7 V. The C_s values obtained are 153.43, 123, 114.4, 109.4, and 106.4 F/g for 1, 2, 3, 4, and 5 A/g, respectively (Figure 10b). The C_s after 500 cycles was measured at a current density of 3 and 5 A/g, for which **Comp2** showed an activity of 106 and 87 F/g, respectively. The GCD curves of 3 and 5 A/g show 7.3% and 18.2% of degradation in the activity. The CV curves were recorded between −0.6 and 0.2 V at scan rates ranging from 20, 30, 50, 75, to 100 mV, and the specific

capacitance values calculated were 395, 360, 363, 367, and 370 F/g, respectively (Figure S13). The sample's CV was collected at 50 mV and 100 mV per second scan rate after ADT, and the C_s values obtained were 243 and 164 F/g. The CV curves show a 33% and 55% degradation in the specific capacitance, respectively. The good specific capacitance values obtained for both the compounds at decent current densities indicate that such hybrids pose good potential for electrochemical super-capacitance. However, the degradation of the pseudocapaci-tance properties were drastic for **Comp1** and much less for **Comp2**, the issues associated with which must be addressed in future works.

4. CONCLUSION

Two twin isostructural POMOF hybrids, based on the Keggin ions ($PMo_{12}O_{40}^{3-}$ and $PW_{12}O_{40}^{3-}$), were synthesized through hydrothermal routes by thorough standardization of synthetic pH conditions. Crystal structure analyses revealed that the hybrids have identical 3D architectures primarily formed of Cu-bp chains with POMs acting as anionic ligands for growing the structures. Noncovalent interactions like H-bonding, CH-π interactions were instrumental in stabilizing the 3D hybrid structure. The compounds were nonmagnetic, and the chemical states of the metals ions were extensively probed through different spectroscopic techniques in relevance to their roles in catalytic activities. The compounds were found to be semiconducting in nature with optical band gap lying in the visible range. The heterogeneous catalytic property studies on the compounds revealed that they are highly active for small-molecule oxidation, with **Comp2** showing marginally better activity than **Comp1**, owing to the difference in acidity of the constituting HPA units. Both compounds showed good photocatalytic dye degradation properties on methylene blue under UV irradiation. **Comp2** excelled in terms of both efficiency and kinetic rates, owing to its higher UV absorption properties originating from the POM unit. Finally, the electrochemical and pseudocapacitance properties of the twin hybrids were explored. Both compounds showed good specific capacitance at practical current densities, with **Comp2** showing higher electrocapacitive stability. The detailed structural analyses and close structure-property relationship studies presented in this work will elucidate important aspects of material designs in this class of POMOF hybrids for better catalytic applications in future.

ASSOCIATED CONTENT

S Supporting Information

The CCDC reference numbers for the compounds **Comp1** and **Comp2** are 1847876 and 1847877, respectively. The Supporting Information is available free of charge on the ACS Publications website at DOI: 10.1021/acs.inorgchem.8b01631.

> Details on catalytic studies, the assignments of peaks in IR, figures of structural coordination environments of **Comp1** and **Comp2**, SEM images, and electrochemical plots such as CV and capacitance (PDF)

Accession Codes

CCDC 1847876−1847877 contain the supplementary crystallographic data for this paper. These data can be obtained free of charge via www.ccdc.cam.ac.uk/data_request/cif, or by emailing data_request@ccdc.cam.ac.uk, or by contacting The Cambridge Crystallographic Data Centre, 12 Union Road, Cambridge CB2 1EZ, UK; fax: +44 1223 336033.

AUTHOR INFORMATION

Corresponding Author
*Phone: 080-22082998. Fax: 080-22082627. E-mail: sebastiancp@jncasr.ac.in.

ORCID
Sebastian C. Peter: 0000-0002-5211-446X

Notes
The authors declare no competing financial interest.

ACKNOWLEDGMENTS

REFERENCES

(1) Yuan, S. A.; Zou, L. F.; Qin, J. S.; Li, J. L.; Huang, L.; Feng, L. A.; Wang, X. A.; Bosch, M.; Alsalme, A.; Cagin, T.; Zhou, H. C. Construction of hierarchically porous metal-organic frameworks through linker labilization. *Nat. Commun.* **2017**, *8*, 15356.
(2) Kim, H.; Yang, S.; Rao, S. R.; Narayanan, S.; Kapustin, E. A.; Furukawa, H.; Umans, A. S.; Yaghi, O. M.; Wang, E. N. Water harvesting from air with metal-organic frameworks powered by natural sunlight. *Science* **2017**, *356*, 430−432.
(3) Sartorel, A.; Carraro, M.; Scorrano, G.; De Zorzi, R.; Geremia, S.; McDaniel, N. D.; Bernhard, S.; Bonchio, M. Polyoxometalate embedding of a tetraruthenium(IV)-oxo-core by template-directed metalation of [gamma-SiW₁₀O₃₆]⁸⁻ A totally inorganic oxygen-evolving catalyst. *J. Am. Chem. Soc.* **2008**, *130*, 5006−5007.
(4) Kikukawa, Y.; Yamaguchi, K.; Mizuno, N. Zinc(II) Containing gamma-Keggin Sandwich-Type Silicotungstate: Synthesis in Organic Media and Oxidation Catalysis. *Angew. Chem., Int. Ed.* **2010**, *49*, 6096−6100.
(5) Gouzerh, P.; Proust, A. Main-group element, organic, and organometallic derivatives of polyoxometalates. *Chem. Rev.* **1998**, *98*, 77−111.

(6) Wang, S. S.; Yang, G. Y. Recent Advances in Polyoxometalate-Catalyzed Reactions. *Chem. Rev.* **2015**, *115*, 4893−4962.
(7) Getman, R. B.; Bae, Y. S.; Wilmer, C. E.; Snurr, R. Q. Review and Analysis of Molecular Simulations of Methane, Hydrogen, and Acetylene Storage in Metal-Organic Frameworks. *Chem. Rev.* **2012**, *112*, 703−723.
(8) Long, D. L.; Burkholder, E.; Cronin, L. Polyoxometalate clusters, nanostructures and materials: From self assembly to designer materials and devices. *Chem. Soc. Rev.* **2007**, *36*, 105−121.
(9) Lydon, C.; Busche, C.; Miras, H. N.; Delf, A.; Long, D. L.; Yellowlees, L.; Cronin, L. Nanoscale Growth of Molecular Oxides: Assembly of a {V₆} Double Cubane Between Two Lacunary {P₂W₁₅} Polyoxometalates. *Angew. Chem., Int. Ed.* **2012**, *51*, 2115−2118.
(10) Bosch-Navarro, C.; Matt, B.; Izzet, G.; Romero-Nieto, C.; Dirian, K.; Raya, A.; Molina, S. I.; Proust, A.; Guldi, D. M.; Marti-Gastaldo, C.; Coronado, E. Charge transfer interactions in self-assembled single walled carbon nanotubes/Dawson-Wells polyoxometalate hybrids. *Chem. Sci.* **2014**, *5*, 4346−4354.
(11) Sadakane, M.; Steckhan, E. Electrochemical properties of polyoxometalates as electrocatalysts. *Chem. Rev.* **1998**, *98*, 219−237.
(12) Genovese, M.; Lian, K. Polyoxometalate modified inorganic-organic nanocomposite materials for energy storage applications: A review. *Curr. Opin. Solid State Mater. Sci.* **2015**, *19*, 126−137.
(13) Katsoulis, D. E. A survey of applications of polyoxometalates. *Chem. Rev.* **1998**, *98*, 359−387.
(14) Ye, T. L.; Wang, J. H.; Dong, G. H.; Jiang, Y. X.; Feng, C.; Yang, Y. L. Recent Progress in the Application of Polyoxometalates for Dye-sensitized/Organic Solar Cells. *Chin. J. Chem.* **2016**, *34*, 747−756.
(15) Ruiz, V.; Suarez-Guevara, J.; Gomez-Romero, P. Hybrid electrodes based on polyoxometalate-carbon materials for electrochemical supercapacitors. *Electrochem. Commun.* **2012**, *24*, 35−38.
(16) El Moll, H.; Black, F. A.; Wood, C. J.; Al-Yasari, A.; Marri, A. R.; Sazanovich, I. V.; Gibson, E. A.; Fielden, J. Increasing p-type dye sensitised solar cell photovoltages using polyoxometalates. *Phys. Chem. Chem. Phys.* **2017**, *19*, 18831−18835.
(17) Boulmier, A.; Vacher, A.; Zang, D. J.; Yang, S.; Saad, A.; Marrot, J.; Oms, O.; Mialane, P.; Ledoux, I.; Ruhlmann, L.; Lorcy, D.; Dolbecq, A. Anderson-Type Polyoxometalates Functionalized by Tetrathiafulvalene Groups: Synthesis, Electrochemical Studies, and NLO Properties. *Inorg. Chem.* **2018**, *57*, 3742−3752.
(18) Roy, S.; Sarkar, S.; Pan, J.; Waghmare, U. V.; Dhanya, R.; Narayana, C.; Peter, S. C. Crystal Structure and Band Gap Engineering in Polyoxometalate-Based Inorganic-Organic Hybrids. *Inorg. Chem.* **2016**, *55*, 3364−3377.
(19) Miras, H. N.; Vila-Nadal, L.; Cronin, L. Polyoxometalate based open-frameworks (POM-OFs). *Chem. Soc. Rev.* **2014**, *43*, 5679−5699.
(20) Song, J.; Luo, Z.; Britt, D. K.; Furukawa, H.; Yaghi, O. M.; Hardcastle, K. I.; Hill, C. L. A Multiunit Catalyst with Synergistic Stability and Reactivity: A Polyoxometalate-Metal Organic Framework for Aerobic Decontamination. *J. Am. Chem. Soc.* **2011**, *133*, 16839−16846.
(21) Han, Q. X.; He, C.; Zhao, M.; Qi, B.; Niu, J. Y.; Duan, C. Y. Engineering Chiral Polyoxometalate Hybrid Metal-Organic Frameworks for Asymmetric Dihydroxylation of Olefins. *J. Am. Chem. Soc.* **2013**, *135*, 10186−10189.
(22) Sun, C. Y.; Liu, S. X.; Liang, D. D.; Shao, K. Z.; Ren, Y. H.; Su, Z. M. Highly Stable Crystalline Catalysts Based on a Microporous Metal-Organic Framework and Polyoxometalates. *J. Am. Chem. Soc.* **2009**, *131*, 1883−1888.
(23) Liu, D.; Lu, Y.; Tan, H. Q.; Chen, W. L.; Zhang, Z. M.; Li, Y. G.; Wang, E. B. Polyoxometalate-based purely inorganic porous frameworks with selective adsorption and oxidative catalysis functionalities. *Chem. Commun.* **2013**, *49*, 3673−3675.
(24) He, W. W.; Li, S. L.; Zang, H. Y.; Yang, G. S.; Zhang, S. R.; Su, Z. M.; Lan, Y. Q. Entangled structures in polyoxometalate-based coordination polymers. *Coord. Chem. Rev.* **2014**, *279*, 141−160.

(25) Du, D. Y.; Qin, J. S.; Li, S. L.; Su, Z. M.; Lan, Y. Q. Recent advances in porous polyoxometalate-based metal-organic framework materials. *Chem. Soc. Rev.* **2014**, *43*, 4615−4632.

(26) Li, T. H.; Li, Q. G.; Yan, J.; Li, F. Facile fabrication of corrosion-resistant superhydrophobic and superoleophilic surfaces with MnWO4:Dy3+ microbouquets. *Dalton Trans.* **2014**, *43*, 5801−5805.

(27) Li, T. H.; Li, Q. G.; Yan, J.; Li, F. Photocatalytic degradation of organic dyes by La^{3+}/Ce^{3+}-H$_3$PW$_{12}$O$_{40}$ under different light irradiation. *Dalton Trans.* **2014**, *43*, 9061−9069.

(28) Chen, Z. Y.; Lu, J. H.; Yu, K.; Zhang, H.; Wang, L.; Wang, C. M.; Zhou, B. B. Nonclassical Phosphomolybdates with Different Degrees of Reduction: Syntheses and Structural and Photo/Electrocatalytic Properties. *Inorg. Chem.* **2016**, *55*, 8309−8320.

(29) Zhang, X. M.; Wu, H. S.; Zhang, F. Q.; Prikhod'ko, A.; Kuwata, S.; Comba, P. The three-electron heteropoly blue [P$_6$Mo$_{18}$O$_{73}$]$^{11−}$ with a basket-shaped skeleton. *Chem. Commun.* **2004**, 2046−2047.

(30) Schonweiz, S.; Sorsche, D.; Schwarz, B.; Rau, S.; Streb, C. Structural and reactivity insights into covalently linked Cu(I) complex-Anderson polyoxometalates. *Dalton Trans.* **2017**, *46*, 9760−9764.

(31) Iyer, A. K.; Roy, S.; Haridasan, R.; Sarkar, S.; Peter, S. C. Ligand mediated valence fluctuation of copper in new hybrid materials constructed from decavanadate and a Cu(1,10-phenanthroline) complex. *Dalton Trans.* **2014**, *43*, 2153−2160.

(32) Roy, S.; Mumbaraddi, D.; Jain, A.; George, S. J.; Peter, S. C. Crystal Engineering in Supramolecular Polyoxometalate Hybrids through pH Controlled in Situ Ligand Hydrolysis. *Inorg. Chem.* **2018**, *57*, 590−601.

(33) Kozhevnikov, I. *Catalysis by Polyoxometalates*; Wiley: 2002; Vol. 2, p 220.

(34) Kholdeeva, O. A.; Vanina, M. P.; Timofeeva, M. N.; Maksimovskaya, R. I.; Trubitsina, T. A.; Melgunov, M. S.; Burgina, E. B.; Mrowiec-Bialon, J.; Jarzebski, A. B.; Hill, C. L. Co-containing polyoxometalate-based heterogeneous catalysts for the selective aerobic oxidation of aldehydes under ambient conditions. *J. Catal.* **2004**, *226*, 363−371.

(35) Ren, Y. H.; Wang, M. Y.; Chen, X. Y.; Yue, B.; He, H. Y. Heterogeneous Catalysis of Polyoxometalate Based Organic-Inorganic Hybrids. *Materials* **2015**, *8*, 1545−1567.

(36) Martín-Caballero, J.; San José Wéry, A.; Reinoso, S.; Artetxe, B.; San Felices, L.; El Bakkali, B.; Trautwein, G.; Alcañiz-Monge, J.; Vilas, J. L.; Gutiérrez-Zorrilla, J. M. A Robust Open Framework Formed by Decavanadate Clusters and Copper(II) Complexes of Macrocyclic Polyamines: Permanent Microporosity and Catalytic Oxidation of Cycloalkanes. *Inorg. Chem.* **2016**, *55*, 4970−4979.

(37) Ma, Y.; Peng, H.; Liu, J.; Wang, Y.; Hao, X.; Feng, X.; Khan, S. U.; Tan, H.; Li, Y. Polyoxometalate-Based Metal−Organic Frameworks for Selective Oxidation of Aryl Alkenes to Aldehydes. *Inorg. Chem.* **2018**, *57*, 4109−4116.

(38) Han, Q.; Sun, X.; Li, J.; Ma, P.; Niu, J. Novel Isopolyoxotungstate [H$_2$W$_{11}$O$_{38}$]$^{8−}$ Based Metal Organic Framework: As Lewis Acid Catalyst for Cyanosilylation of Aromatic Aldehydes. *Inorg. Chem.* **2014**, *53*, 6107−6112.

(39) Dieterle, M.; Weinberg, G.; Mestl, G. Raman spectroscopy of molybdenum oxides - Part I. Structural characterization of oxygen defects in MoO(3-x) by DR UV/VIS, Raman spectroscopy and X-ray diffraction. *Phys. Chem. Chem. Phys.* **2002**, *4*, 812−821.

(40) Zhou, Y.; Chen, G. J.; Long, Z. Y.; Wang, J. Recent advances in polyoxometalate-based heterogeneous catalytic materials for liquid-phase organic transformations. *RSC Adv.* **2014**, *4*, 42092−42113.

(41) Lu, B. B.; Yang, J.; Che, G. B.; Pei, W. Y.; Ma, J. F. Highly Stable Copper(I)-Based Metal-Organic Framework Assembled with Resorcin[4]arene and Polyoxometalate for Efficient Heterogeneous Catalysis of Azide-Alkyne "Click" Reaction. *ACS Appl. Mater. Interfaces* **2018**, *10*, 2628−2636.

(42) Kholdeeva, O. A.; Maksimchuk, N. V.; Maksimov, G. M. Polyoxometalate-based heterogeneous catalysts for liquid phase selective oxidations Comparison of different strategies. *Catal. Today* **2010**, *157*, 107−113.

(43) Vasylyev, M. V.; Neumann, R. New heterogeneous polyoxometalate based mesoporous catalysts for hydrogen peroxide mediated oxidation reactions. *J. Am. Chem. Soc.* **2004**, *126*, 884−890.

(44) Zeng, L.; Xiao, L.; Long, Y. K.; Shi, X. W. Trichloroacetic acid-modulated synthesis of polyoxometalate@UiO-66 for selective adsorption of cationic dyes. *J. Colloid Interface Sci.* **2018**, *516*, 274−283.

(45) Yagub, M. T.; Sen, T. K.; Afroze, S.; Ang, H. M. Dye and its removal from aqueous solution by adsorption: A review. *Adv. Colloid Interface Sci.* **2014**, *209*, 172−184.

(46) Chen, C.; Zhang, M.; Guan, Q. X.; Li, W. Kinetic and thermodynamic studies on the adsorption of xylenol orange onto MIL-101 (Cr). *Chem. Eng. J.* **2012**, *183*, 60−67.

(47) Haque, E.; Lo, V.; Minett, A. I.; Harris, A. T.; Church, T. L. Dichotomous adsorption behaviour of dyes on an amino-functionalised metal-organic framework, amino-MIL-101(Al). *J. Mater. Chem. A* **2014**, *2*, 193−203.

(48) Zhao, X.; Zhang, S.; Yan, J.; Li, L.; Wu, G.; Shi, W.; Yang, G.; Guan, N.; Cheng, P. Polyoxometalate-Based Metal−Organic Frameworks as Visible-Light-Induced Photocatalysts. *Inorg. Chem.* **2018**, *57*, 5030−5037.

(49) Fielden, J.; Sumliner, J. M.; Han, N. N.; Geletii, Y. V.; Xiang, X.; Musaev, D. G.; Lian, T. Q.; Hill, C. L. Water splitting with polyoxometalate-treated photoanodes: enhancing performance through sensitizer design. *Chem. Sci.* **2015**, *6*, 5531−5543.

(50) Wang, M.; et al. An overall water-splitting polyoxometalate catalyst for the electromicrobial conversion of CO2 in neutral water. *J. Mater. Chem. A* **2018**, *6*, 9915−9921.

(51) Wang, X. L.; Zhang, H. X.; Wang, X.; Zhang, S.; Liu, J. H.; Lin, H. Y.; Liu, G. C. A novel two-fold interpenetrating 3D metal-organic framework based on Lindqvist-type hexamolybdate: Synthesis, structure, electrochemical and photocatalytic properties. *Inorg. Chem. Commun.* **2018**, *88*, 60−64.

(52) *SAINT 6.02*; Bruker AXS Inc.: Madison, WI, 2000.

(53) Sheldrick, G. M. *SADABS*, Empirical Absorption Correction Program; University of Göttingen: Germany, 1997.

(54) Sheldrick, G. M.; Schneider, T. R. SHELXL: High-resolution refinement. *Methods Enzymol.* **1997**, *277*, 319−343.

(55) Spek, A. L. Single-crystal structure validation with the program PLATON. *J. Appl. Crystallogr.* **2003**, *36*, 7−13.

(56) Dolomanov, O. V.; Bourhis, L. J.; Gildea, R. J.; Howard, J. A. K.; Puschmann, H. OLEX2: a complete structure solution, refinement and analysis program. *J. Appl. Crystallogr.* **2009**, *42*, 339−341.

(57) Farrugia, L. *J. Appl. Crystallogr.* **1999**, *32*, 837−838.

(58) Choi, J. G.; Thompson, L. T. XPS study of as-prepared and reduced molybdenum oxides. *Appl. Surf. Sci.* **1996**, *93*, 143−149.

(59) Ji, W. X.; Shen, R.; Yang, R.; Yu, G. Y.; Guo, X. F.; Peng, L. M.; Ding, W. P. Partially nitrided molybdenum trioxide with promoted performance as an anode material for lithium-ion batteries. *J. Mater. Chem. A* **2014**, *2*, 699−704.

(60) Gomes, W. C. M.; Neto, A. d. O. W.; Pimentel, P. M.; Melo, D. M. d. A.; Silva, F. R. G. e. An in situ X-ray absorption spectroscopy study of copper nanoparticles in microemulsion. *Colloids Surf., A* **2013**, *426*, 18−25.

(61) Vasylyev, M. V.; Neumann, R. New heterogeneous polyoxometalate based mesoporous catalysts for hydrogen peroxide mediated oxidation reactions. *J. Am. Chem. Soc.* **2004**, *126*, 884−890.

(62) Hill, C. L. Progress and challenges in polyoxometalate-based catalysis and catalytic materials chemistry. *J. Mol. Catal. A: Chem.* **2007**, *262*, 2−6.

(63) Yang, X. Y.; Zhang, H. F.; Li, S. X.; Sha, J. Q.; Li, X.; Ma, F. Study about the highest connected twin Keggin POMs based hybrid compound: Synthesis, PPy loading, physical absorption and visible-light photogradation for organic pollutant. *Polyhedron* **2018**, *144*, 240−248.

(64) Bu, Y.; Liu, R.; Zhen, M.; Li, F.; Sun, Z.; Xu, L. A hybrid compound containing polyoxoanions and organic dye cations with

visible-light photocatalytic H2 evolution activity. *Inorg. Chem. Commun.* **2015**, *62*, 34.

(65) Youn, M. H.; Kim, H.; Jung, J. C.; Song, I. K.; Barteau, K. P.; Barteau, M. A. UV-vis spectroscopy studies of H3PMo12-XWXO40 heteropolyacid (HPA) catalysts in the solid state: Effects of water content and polyatom substitution. *J. Mol. Catal. A: Chem.* **2005**, *241*, 227−232.

(66) Wang, X. L.; Li, N.; Tian, A. X.; Ying, J.; Li, T. J.; Lin, X. L.; Luan, J.; Yang, Y. Unprecedented Application of Flexible Bis(pyridyl-tetrazole) Ligands To Construct Helix/Loop Subunits To Modify Polyoxometalate Anions. *Inorg. Chem.* **2014**, *53*, 7118−7129.

(67) Cai, H. H.; Lu, J. H.; Yu, K.; Zhang, H.; Wang, C. M.; Wang, L.; Zhou, B. B. Organic-inorganic hybrid supramolecular assembly through the highest connectivity of a Wells-Dawson molybdoarsenate. *Inorg. Chem. Commun.* **2015**, *62*, 24−28.

(68) Zhou, X. J.; Ji, Y. X.; Cao, J. F.; Xin, Z. F. Polyoxometalate encapsulated in metal-organic gel as an efficient catalyst for visible-light-driven dye degradation applications. *Appl. Organomet. Chem.* **2018**, *32*, e4206.

(69) Toth, J. E.; Anson, F. C. Electrocatalytic Reduction of Nitrite and Nitric-Oxide to Ammonia with Iron-Substituted Polyoxotung-states. *J. Am. Chem. Soc.* **1989**, *111*, 2444−2451.

(70) Dong, S. J.; Xi, X. D.; Tian, M. Study of the Electrocatalytic Reduction of Nitrite with Silicotungstic Heteropolyanion. *J. Electroanal. Chem.* **1995**, *385*, 227−233.

(71) Keita, B.; Belhouari, A.; Nadjo, L.; Contant, R. Electrocatalysis by Polyoxometalate Polymer Systems - Reduction of Nitrite and Nitric-Oxide. *J. Electroanal. Chem.* **1995**, *381*, 243−250.

(72) Toth, J. E.; Anson, F. C. Electrochemical Properties of Iron(Iii)-Substituted Heteropolytungstate Anions. *J. Electroanal. Chem. Interfacial Electrochem.* **1988**, *256*, 361−370.

(73) Conway, B. E. *Electrochemical Pseudocapacitors*; Springer Science: New York, 1999.

(74) Brousse, T.; Belanger, D.; Long, J. W. To Be or Not To Be Pseudocapacitive? *J. Electrochem. Soc.* **2015**, *162*, A5185−A5189.